Supplemental Information

Surface Charge, Electroosmotic Flow and DNA Extension in Chemically Modified Thermoplastic Nanoslits and Nanochannels

Franklin I. Uba,[1,6] Swathi R. Pullagurla,[3] Nichanun Sirasunthorn,[5] Jiahao Wu,[4] Sunggook Park,[4] Rattikan Chantiwas,[5] Yoonkyoung Cho,[6] Heungjoo Shin[6] and Steven A. Soper[1, 2, 4, 6*]

[1]Department of Chemistry, UNC-Chapel Hill, NC, 27599
[2]Department of Biomedical Engineering, UNC-Chapel Hill, NCSU, Raleigh, NC
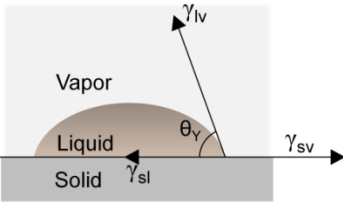[3]Department of Chemistry, Louisiana State University, Baton-Rouge, LA, 70803
[4]Department of Mechanical Engineering, Louisiana State University, Baton-Rouge, LA
[5]Department of Chemistry, Mahidol University, Bangkok, Thailand
[6] Department of Chemistry and Center of Excellence for Innovation in Chemistry, Faculty of Science, Mahidol University, Bangkok, Thailand

*corresponding author ssoper@unc.edu

Effects of thermal fusion bonding temperature on the wettability of O_2-PMMA. Previous reports have shown that the temperature used to thermally fusion bond a cover plate to a nanofluidic substrate affects the surface wettability/solid surface tension of plasma treated polymer surfaces.[1] We therefore investigated the effects of temperature on the wettability of O_2-PMMA (50 W, 5.5 sccm gas flow rate for 35 s) by measuring the water contact angle at temperatures between 75°C and 100°C, the typical temperature range utilized for thermal assembly of PMMA nanofluidic devices. As reported by Chai et al.[2] the interpretation of contact angles in terms of the wettability relies on the validity of Young's equation, which interrelates the Young's contact angle, θ_Y, with the interfacial tension of a liquid-vapor, γ_{lv}, solid-vapor, γ_{sv}, and solid-liquid, γ_{sl} (see equation S1 and Figure S1);

$$\cos\theta_Y = \frac{\gamma_{sv} - \gamma_{sl}}{\gamma_{lv}}$$

(S1)

Figure S1. Schematic showing the interfacial tensions in Young's equation.

Typically, θ_Y is expected to be a good approximation of the measured contact angle for a surface when the RMS roughness ≤ 5 nm.[3] γ_{sl} can be determined by;[3]

$$\gamma_{sl} = \gamma_{lv} + \gamma_{sv} - 2\sqrt{\gamma_{lv}\gamma_{sv}}(1 - \beta(\gamma_{lv} - \gamma_{sv})^2)$$

(S2)

γ_{sv} can be calculated using the water contact angle and equations S1 and S2;

$$\gamma_{sv} \left(1 - \beta(\gamma_{lv} - \gamma_{sv})^2\right) = \frac{\left[\gamma_{lv} \left(1 + \cos\theta_Y\right)\right]^2}{4\,\gamma_{lv}}$$

(S3)

where β is 1.057×10^{-4} $(m^2/mJ)^2$ and γ_{lv} for water is 72.70 mJ/m^2.

As shown in Figure S2a, there was a gradual increase in the water contact angle as the temperature of the plasma treated PMMA was increased. Heating the plasma treated substrate to temperatures $\leq 80°C$ did not result in a significant change in the surface wettability. However, at temperatures $\geq 85°C$, there was a significant increase in γ_{sl}. As described by Jackson et al.,[1] this increase arises because the functional groups generated after plasma treatment (≤ 10 nm from the surface) undergo thermally induced rearrangement and are buried into the bulk substrate when heated to elevated temperatures. To avoid this, we performed fusion bonding of devices at 80°C for 400 s. The wettability was primarily retained using these conditions and allowed the device to fill easily with aqueous solvents by capillary action and low pressure suction.
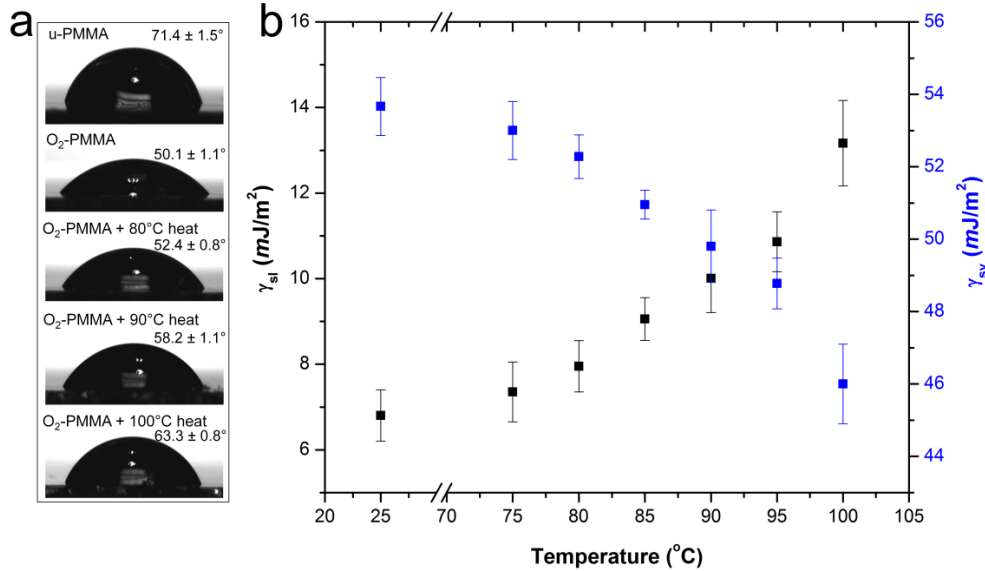
Figure S2. Variation of the water contact angle (a) and surface tension forces (b) with temperature for O_2-PMMA. Planar PMMA pieces were activated using an O_2 plasma with the following conditions; power level of 50 W, 5.5 sccm gas flow rate and treatment time of 35 s. Each reported value represents the average of five values measured at different positions on the substrate and the vertical bars represent one standard deviation unit.

3

Surface Energy (SE) of u-PMMA and O$_2$-PMMA surfaces. As proposed by Zisman,[4] the SE of a solid surface can be estimated by measuring the contact angle of a series of liquids with known γ_{lv}. A graph of the water contact angles as a function of γ_{lv} is called a Zisman plot. The liquid-vapor surface tension at $\cos\theta_Y = 1$, also called the critical surface tension, γ_c, gives the SE of the solid surface. A test liquid with $\gamma_{lv} \sim \gamma_c$ will completely spread over the surface. Figure S3 shows Zisman plots for u- and O$_2$-PMMA. The graph was generated by depositing 2.0 µl of three liquids, water ($\gamma_{lv} \sim 72.80$ mJ/m^2), glycerol ($\gamma_{lv} \sim 64.00$ *m*J/m^2) and DMSO ($\gamma_{lv} \sim 43.54$ *m*J/m^2) onto the solid surface. The results revealed that the SE increased from ~27.02 *m*J/m^2 for u-PMMA to 38.88 *m*J/m^2 after plasma treatment suggesting the incorporation of oxygen containing polar functional groups onto the polymer surface. We speculate that this will approximately be the SE experienced in the plasma modified nanoslit and nanochannels and, as suggested from the previous section, expect it to remain relatively unchanged after device assembly when the assembly temperature was ≤80º.
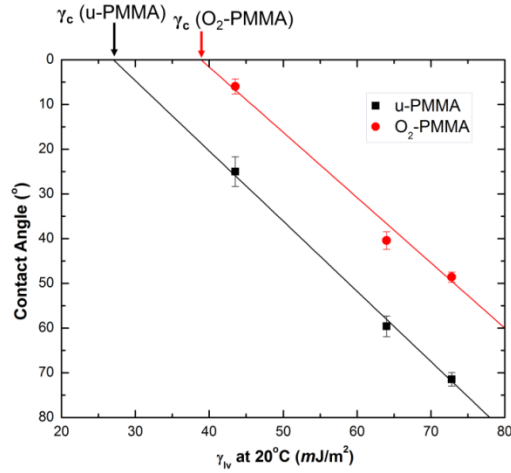
Figure S3. Zisman plot for u-PMMA (black trace) and O$_2$-PMMA (red trace) measured with water ($\gamma_{lv} \sim 72.80$ mJ/m^2), glycerol ($\gamma_{lv} \sim 64.00$ *m*J/m^2) and DMSO ($\gamma_{lv} \sim 43.54$ *m*J/m^2). Each point represents the average of five values measured at different positions on the substrate and the vertical bars represent one standard deviation unit.

X-ray Photoelectron Spectroscopy (XPS) analysis of plasma treated PMMA substrates and nanoslits. For XPS measurements, C1s, O1s and N1s photoelectron signals were acquired using

an Axis Ultra DLD X-ray photoelectron spectrometer (Kratos Analytical) under ultra-high vacuum conditions (10^{-8} to 10^{-10} Torr) with a monochromatic Al Kα X-ray source, 20 eV pass energy, 370 s acquisition time, 1,600 ms dwell time and 20° electron take-off angle. Given an inelastic mean free path of 3-4 nm, ~95% of the resultant signal originated 9-12 nm from the surface.[5-7] For all XPS spectra, Shirley backgrounds were subtracted by averaging at least 10 data points associated with the background.

As shown in Figure S4a for planar PMMA surfaces, O_2-PMMA led to an increase in the O/C ratio confirming the generation of oxygen-containing groups.[2] For amination of the O_2-PMMA, several conditions involving EDC or EDC-NHS coupling chemistries were evaluated with concentrations ranging between 0.1 and 1 M ethylene diamines (EDA). In all cases, there were decreases in the O/C ratios (Figure S4a); however, depending on the amination conditions, the amount of N-containing groups differed. As depicted in Figure S2b, the highest N/C ratio was observed for animation involving the reaction of O_2-PMMA with 1 M EDA in EDC.

To identify the surface functionalities generated after the O_2-PMMA, the C1s spectra were processed based on previously published work.[8] The u-PMMA C1s spectrum showed the presence of four Gaussian components: (1) 284.6 eV aliphatic C-C and C-H; (2) 285.2 eV quaternary C-C α to the pristine ester; (3) 286.4 eV methoxy C-O ester; and (4) 288.7 eV carbonyl C=O ester (Figure S2c). This fitting was in good agreement with previous literature. Nevertheless, the theoretical peak area ratio of the C1s components (1) - (4) of 2:1:1:1 was found to be 1.90:1.18:1.20:1.00 in our data. The slight deviation may have been attributed to additives and/or plasticizers introduced into the substrate by the manufacturer.[9] Furthermore, in addition to the peaks listed above for u-PMMA, the deconvoluted C1s peak of O_2-PMMA showed the presence of a peak at a binding energy of 289.7 eV (Figure S4d). This peak corresponded to the

OC=O of a carboxylic acid. After amination, the deconvoluted C1s peak showed the absence of the carboxylic acid peak and the presence of two peaks; (1) 285.8 eV, C-N bond of an amine, and (2) 287.9 eV O=C-N bond of an amide (Figure S4e).

The combined survey spectra are shown in Figure S4f for an unassembled PMMA nanoslit device. The trace for u-PMMA showed the presence of only two peaks at 284.8 eV and 532.0 eV indicative of C1s and O1s core levels, respectively. After exposure to 50 W (5.5 sccm) O_2 plasma for 35 s, there were observable changes in the individual intensities of the C1s and O1s peaks when compared to the u-PMMA (red trace in Figure S4f). There was an increase in the O/C atomic ratio from 0.331 ±0.006 for u-PMMA to 0.403 ±0.003 for O_2-PMMA indicating the incorporation of oxygen containing chemical groups on the PMMA surface. The survey spectrum taken for the NH_2-PMMA surface (blue trace) showed the presence of a new peak centered at 399.69 eV in addition to the C1s and O1s peaks. This peak is characteristic of surfaces possessing nitrogen-containing functionalities (N1s core level).[10,11]

Further analysis of the XPS data revealed that the atomic ratio of the peak area of the O1s peak to the C1s peak was 0.309 ±0.006 with the ratio of the O1s to C1s peak areas ~10.9% less for NH_2-PMMA compared to u-PMMA. This result demonstrated that not only was nitrogen successfully incorporated onto the surface of a PMMA nanoslit, but the amount of oxygen present on the surface was less than what was present for the u-PMMA or O_2-PMMA. The N/C ratio was 0.025 ±0.001. The N1s peak obtained was deconvoluted as shown in Figure S4g. This peak consisted of two individual peaks, one centered at 399.1 eV and the other at 400.9 eV. The peak at the lower binding energy corresponded to the N1s core level of an amine (N1), while the higher energy peak was assigned to an amide (N2).[10]

6

In general the observations in the XPS data indicated the presence of fewer ester groups for O_2-PMMA and NH_2-PMMA. Collectively, these results indicated successful oxidation and amination of the PMMA nanoslit surfaces and were similar to the results secured for the planar PMMA surface.
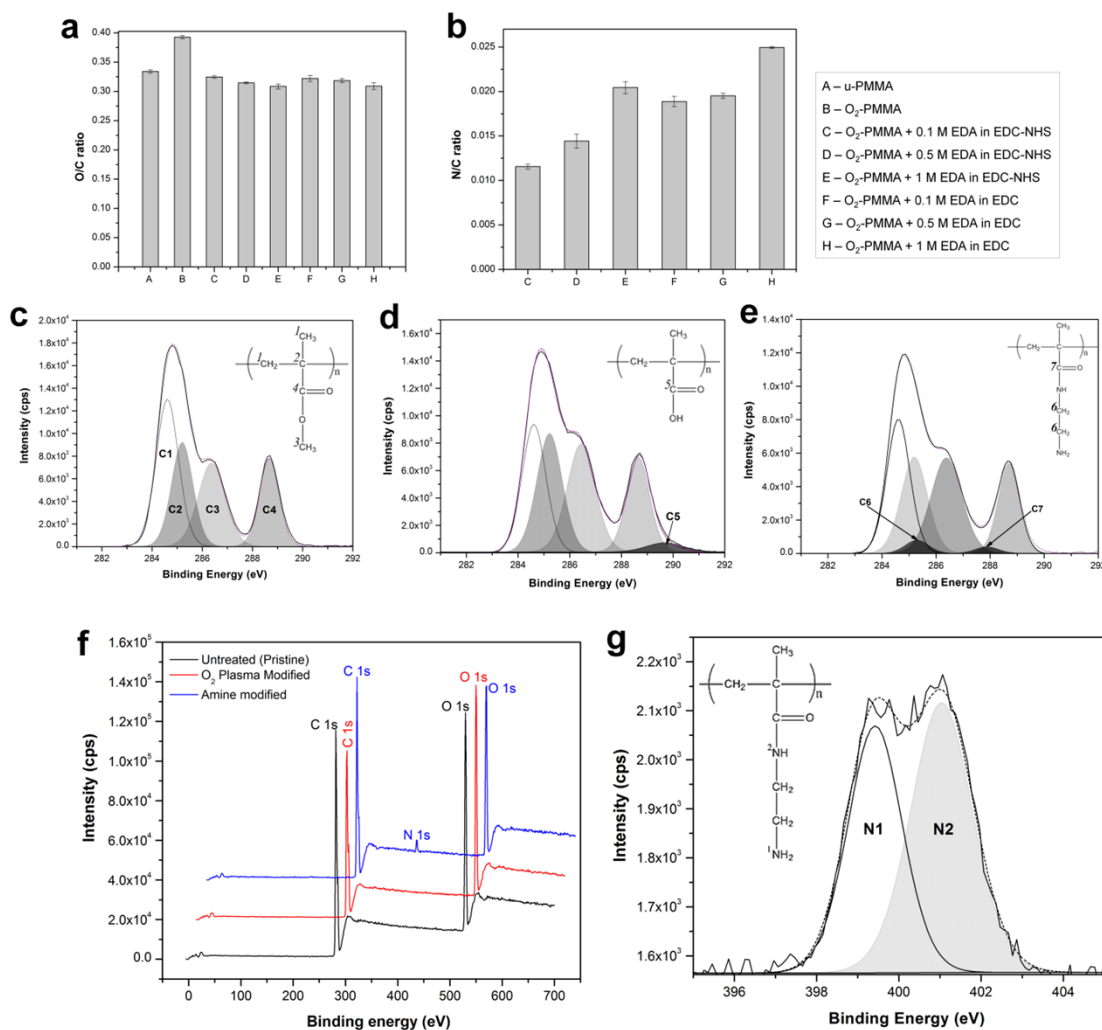

Figure S4. Bar graphs showing (a) O/C and (b) N/C ratios for different surface modification schemes for both u-PMMA (unmodified) and O_2-PMMA (plasma treated PMMA) obtained from XPS data. Deconvoluted C1s spectra for (c) u-PMMA, (d) O_2-PMMA and (e) NH_2-PMMA. PMMA peaks were labeled and assigned to the polymer's monomer. Spectra for the plasma activated PMMA contained an additional peak for carboxyl functionalities and the amine-modified surface showed the presence of two peaks corresponding to the C-N bond of an amine and amide. **(f)** XPS survey spectrum of u-PMMA (black trace), O_2-PMMA (red trace) and NH_2-PMMA (blue trace) nanoslits. (g) N1s deconvoluted spectrum showing two forms of nitrogen atoms. The insert shows the chemical structure of the aminated PMMA surface with the nitrogens labeled N1 and N2.

Fourier Transform Infra-red (FTIR) spectra. To examine the molecular nature of the treated and untreated surfaces, FTIR studies were employed using pre-cut Si wafers coated with a 200 nm Au layer. Commercial PMMA sheets were dissolved in dichloromethane and diluted to yield a solution with a final concentration of 0.5 mg PMMA/mL. This was spin coated onto a Au wafer at 2500 rpm for 60 s to yield a 5 nm thick polymer layer. The coated Au-wafers were allowed to dry in an oven after which they were ready for surface modification and analysis. This approach minimized interference from bulk material in the IR spectra. FTIR spectra were collected at a resolution of 2 cm^{-1} on a 670-IR spectrophotometer (Varian, US) using a monolayer/grazing-angle specular reflectance accessory.

A FTIR spectrum of u-PMMA with the characteristic peaks between 4000 and 650 cm^{-1} is shown in Figure S5a. The most prominent band was v(C=O) at 1733 cm^{-1} assigned to the ester stretch. The absorption bands at 1270, 1241 cm^{-1} and 1195, 1153 cm^{-1} could be assigned to v(C–O) and v(COC) stretching of an ester. This spectrum correlates well with the FTIR spectrum of PMMA documented in the literature.[10] After plasma treatment, there was the appearance of a band at 3430 cm^{-1} and 1700 cm^{-1}, which could be assigned to the v(O-H) and v(C=O) of a carboxylic acid (Figure S5b). Amination with EDA led to the appearance of bands at 3396 cm^{-1} and 1675 cm^{-1} corresponding to the v(N-H) stretch of a primary amine and v(C=O) of an amide (Figure S5c). These support the XPS results and confirm successful surface modification of PMMA using EDA.
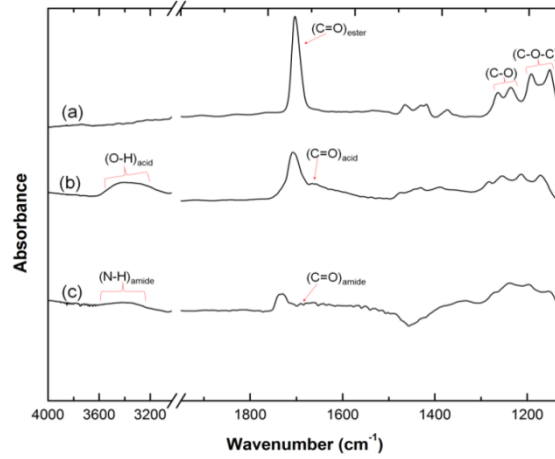
Figure S5. ATR-FTIR spectra for (a) untreated (b) plasma-treated and (c) amine-modified PMMA.

Electrical model of the nanofluidic device. Figure S6a shows the experimental setup of the nanofluidic device configured for making conductance measurements and the equivalent circuit for the nanofluidic device (Figure S6b). The device contained two opposing V-shaped access microchannels (with equal dimensions) with two reservoirs each fabricated at both ends of the microchannel for introducing fluids into the nanochannels or nanoslits. We represented the total voltage applied across reservoirs 1 and 3 as V and the voltage drop across the micro- and nanochannel as V_{mc} and V_{nc}, respectively. In this study, the microchannel dimensions were configured such that most of the voltage drop occurred within the nanochannel. The measured electrical resistance, R, across reservoirs 1 and 3 for a given electrolyte was expressed as a combination of the resistance of the access microchannel, R_{mc}, and the resistance of each nanochannel, R_{nc} (array of parallel resistors each with R_{nc}):

$$R = \frac{R_{nc}}{n} + R_{mc}$$

(S4)

To determine the percent voltage drop across each nanofluidic array, the mixed-scale devices were filled with 0.5 M KCl and the values of R_{mc} and R measured using an Axopatch 200B

9

amplifier. From these values, R_{nc}/n was calculated for the nanoslit (n = 5) and nanochannel (n = 7) using equation (S4) and the percent voltage drop calculated from;

$$\%V = \left[\left(\frac{R_{nc}}{n}\right)\Big/R\right] \times 100$$

(S5)

The data is summarized in Table S1.
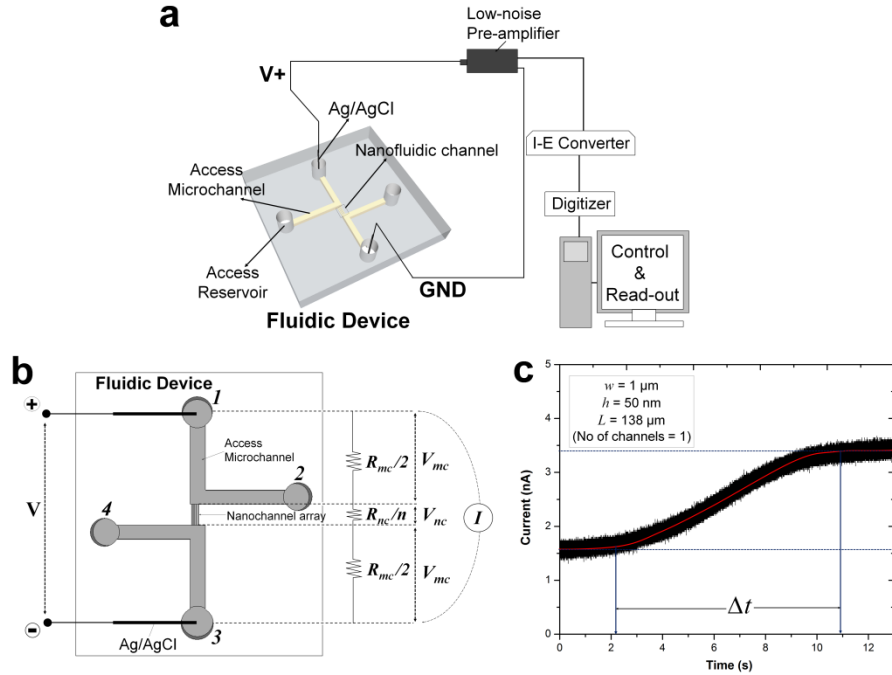
Figure S6. (a) Schematic showing the experimental setup for measuring the resistance of the nanochannels. The nanofluidic device was interfaced to an Axopatch 200B amplifier connected to a Digidata 1440A and computer for readout. Each nanochannel of the array was assumed to have the same geometrical size. (b) Diagram showing the voltage drop and resistances across micro- and nanochannels. (c) Current versus time trace showing the current generated across a nanoslit arising from the replacement of a low ionic strength buffer (0.05 M KCl in 10 mM Tris buffer) with a higher ionic strength buffer (0.1 M KCl in 10 mM Tris) for an O_2-PMMA nanoslit. Buffer replacement within the nanoslit arose from the EOF associated with the device.

Table S1. Measured and calculated electrical resistances across the microchannel R_{mc}, nanoslit/nanochannel R_{nc} and percent voltage drop across nanochannels or nanoslits. The nanofluidic device consisted of a single nanoslit or nanochannel.

Device	Dimensions of Nanofluidic device ($l \times w \times h$)	R_{mc} (kΩ)	R (MΩ)	$\dfrac{R_{nc}}{n}$ (MΩ)	Voltage drop (%V)
Nanoslit	22 μm × 1 μm × 50 nm	501.7 ± 10.2	19.9 ± 1.2	18.9 ± 1.1	95.2 ± 1.1

| Nanochannel | 45 μm × 50 nm × 50 nm | 997.2 ± 12.5 | 60.9 ± 1.8 | 58.9 ± 1.6 | 96.7 ± 1.2 |

Conductance in nanofluidic devices. In the case of fluidic channels, electric currents are a result of the flow of charge carriers (cations and anions of an ionic salt solution). When an external electric field is applied across a nanochannel filled with a salt solution, the total electrical conductance, G_T, neglecting electroosmotic effects is a sum of two components: (1) The bulk conductance (G_B) resulting from the conductivity of the electrolyte solution; and (2) the surface conductance (G_S);

$$G_T \; = \; G_B \; + \; G_S \tag{S6}$$

To derive a mathematical expression for G_T for a nanofluidic device consisting of an array of n nanochannels with width w, height h and length L, filled with a symmetrical electrolyte like KCl, we considered two cases:

(i) High ionic salt concentration - The EDL is very thin (debye length, λ_D, $\leq$ 1% of channel dimension) and the contribution of G_S to G_T becomes negligible. The measured total electric current is a result of ion transport in the bulk solution and the nanoslit/nanochannel can be treated as a simple electrical conductor with bulk conductivity, κ_{bulk} (S/m), expressed as;

$$\kappa_{bulk} = 10^3 \left(\mu_{K^+} \; + \; \mu_{Cl^-} \right) c \, N_A \, e \tag{S7}$$

where μ (m^2 V^{-1} s^{-1}) is the ionic mobility, c (mol/L) is the salt concentration, N_A (mol^{-1}) is Avogadro's number and e is the electron charge. $G_B \, (\approx G_T)$ is represented as;

$$G_B \; = \; \kappa_{bulk} \; \times \; \frac{n \, w \, h}{L}$$

$$\tag{S8}$$

(ii) Low ionic salt concentration – The EDL becomes very thick and overlaps leading to co-ion exclusion effects. The nanoslit/nanochannel becomes predominantly filled with counterions of

11

concentration c_e (mol/L) and the contribution of G_B to G_T becomes negligible (*i.e.* $G_T \approx G_S$). From the principle of conservation of charge, the number of surface charges should be approximately equal to the number of counterions. Therefore, c_e can be represented as;

$$c_e = 10^{-3}\frac{(number\ of\ surface\ charges)}{(volume\ of\ nanochannel)} = \left(\frac{2\,w\,L\,\sigma_s}{e\,N_A} + \frac{2\,h\,L\,\sigma_s}{e\,N_A}\right)\frac{1}{L\,w\,h}$$

$$c_e = 10^{-3}\frac{2\,\sigma_s\,(w + h)}{e\,N_A \cdot w\,h}$$

(S9)

where σ_s is the surface charge density. For a nanoslit, $w \gg h$ and thus, $(w + h) \approx w$. However, for a nanochannel, $w \geq h$; hence, both w and h contribute to c_e and G_S. Therefore, the surface conductivity, κ_{surf} (S/m), is given by;

$$\kappa_{surf} = 10^3\left(\mu_{opp}\right)c_e\,N_A\,e$$

(S10)

where μ_{opp} is the mobility of the counterion (solution cations or anions for the negatively or positively charged surfaces, respectively). Substituting equation S9 into S10, κ_{surf} (S/m) can also be represented in terms of the surface charge density as;

$$\kappa_{surf} = 2\,\mu_{opp}\frac{\sigma_s\,(w + h)}{w\,h}$$

(S11)

And G_S is represented as;

$$G_S = \kappa_{surf} \times \frac{n\,w\,h}{L}$$

(S12)

Therefore, substituting equations S7, S8, S11 and S12 into equation S6, we have;

$$G_T = 10^3 \left(\mu_{K^+} + \mu_{Cl^-} \right) c\, N_A\, e \cdot \frac{n\,w\,h}{L} + 2\,\mu_{opp}\sigma_s\, n\frac{(w\,+\,h)}{L}$$

(S13)

DNA Translocation in amine-modified nanofluidic device. We performed λ-DNA translocations in NH$_2$-PMMA nanofluidic devices at two different pH values, 7.4 (data not shown) and 10.0 (Figure S7). At pH 7.4, λ-DNA molecules were found not to enter the access microchannel due to electrostatic associations of the polyanionic dsDNA to the cationic surface. However, under constant electric field and at pH 10.0, DNA molecules were found to flow smoothly in the access microchannel but were excluded from the nanochannels as seen in Figure S7.
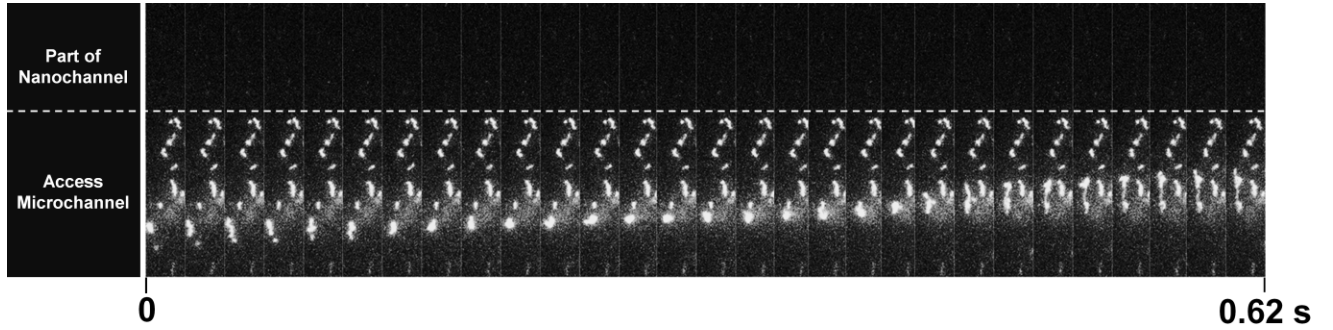
Figure S7. Representative frames of translocation events of λDNA in amine modified nanofluidic devices in the presence of a bias electric field (20 V) in a 2X TBE buffer (pH ≈ 10).

References

1. Jackson, J. M.; Witek, M. A.; Hupert, M. L.; Brady, C.; Pullagurla, S.; Kamande, J.; Aufforth, R. D.; Tignanelli, C. J.; Torphy, R. J.; Yeh, J. J.; Soper, S. A. UV Activation Of Polymeric High Aspect Ratio Microstructures: Ramifications in Antibody Surface Loading for Circulating Tumor Cell Selection. *Lab Chip* 2014, **14**, 106-117.

2. Chai, J.; Lu, F.; Li, B.; Kwok, D. Y. Wettability Interpretation of Oxygen Plasma Modified Poly(methyl methacrylate). *Langmuir* 2004, **20**, 10919-10927.

3. Kwok, D. Y.; Neumann, A. W. Contact Angle Measurement and Contact Angle Interpretation. *Adv. Colloid and Interf. Sci.* 1999, **81**, 167-249.

4. W. A, Z. Relation of The Equilibrium Contact Angle To Liquid and Solid Constitution. In Contact Angle, Wettability, and Adhesion, *ACS.* 1964, **43**, 1-51.

5. Seah, M. P.; Dench, W. A. Quantitative Electron Spectroscopy of Surfaces: A Standard Database for Electron Inelastic Mean Free Paths in Solids. *Surf. Interf. Analysis* 1979, **1**, 2-11.

6.   Mitchell, D. F.; Clark, K. B.; Bardwell, J. A.; Lennard, W. N.; Massoumi, G. R.; Mitchell, I. V. Film Thickness Measurements of SiO_2 by XPS. *Surf. Interf. Analysis* 1994, **21**, 44-50.

7.   Powell, C. J.; Jablonski, A.; Tanuma, S.; Penn, D. R. Effects of Elastic and Inelastic Electron Scattering on Quantitative Surface Analyses by AES and XPS. *J. Elect. Spec. and Related Phen.* 1994, **68**, 605-616.

8.   Seidel, C.; Kopf, H.; Gotsmann, B.; Vieth, T.; Fuchs, H.; Reihs, K. Ar Plasma Treated and Al-Metalized Polycarbonate: a XPS, Mass Spectroscopy and SFM Study. *Appl. Surf. Sci.* 1999, **150**, 19-33.

9.   Ben, A. S.; Baud, G.; Jacquet, M.; Nanse, G.; Fioux, P.; Nardin, M. XPS Characterization of Plasma-Treated and Alumina-Coated PMMA. *Appl. Surf. Sci.* 2000, **153**, 172-183.

10.   Henry, A. C.; Tutt, T. J.; Galloway, M.; Davidson, Y. Y.; McWhorter, C. S.; Soper, S. A.; McCarley, R. L. Surface Modification of Poly(methyl methacrylate) Used in The Fabrication of Microanalytical Devices. *Anal. Chem.* 2000, **72**, 5331-5337.

11.   Gröning, P.; Collaud, M.; Dietler, G.; Schlapbach, L. Plasma Modification of Polymethylmethacrylate and Polyethyleneterephthalate Surfaces. *J. Appl. Phys.* 1994, **76**, 887-892.